

*Electronic Supplementary Information (ESI)*

**Beneficial Synergy of Adsorption-Intercalation-Conversion Mechanisms in Nb<sub>2</sub>O<sub>5</sub>@Nitrogen-Doped Carbon Frameworks for Promoted Removal of Metal Ions via Hybrid Capacitive Deionization**

Guizhi Wang<sup>†</sup>, Tingting Yan<sup>†</sup>, Junjie Shen<sup>‡</sup>, Jianping Zhang<sup>†</sup>, Liyi Shi<sup>†</sup>, and Dongsong Zhang<sup>\*†</sup>

<sup>†</sup> *State Key Laboratory of Advanced Special Steel, School of Materials Science and Engineering, International Joint Laboratory of Catalytic Chemistry, Research Center of Nano Science and Technology, Department of Chemistry, College of Sciences, Shanghai University, No.99 Shangda Road, Shanghai, 200444, China.*

<sup>‡</sup> *Department of Chemical Engineering, University of Bath, Bath BA2 7AY, UK*

<sup>\*</sup> *E-mail: dszhang@shu.edu.cn; Tel: +86 21 66137152.*

The ESI includes 35 pages, 22 figures, and 4 tables.

## Table of contents

<b>Experiments</b> .....	S4
Materials .....	S4
Structural characterization .....	S4
Electrochemical characterization.....	S5
CDI test .....	S6
<b>Figure S1</b> .....	S9
<b>Figure S2</b> .....	S10
<b>Figure S3</b> .....	S11
<b>Figure S4</b> .....	S12
<b>Figure S5</b> .....	S13
<b>Figure S6</b> .....	S14
<b>Figure S7</b> .....	S15
<b>Figure S8</b> .....	S16
<b>Figure S9</b> .....	S17
<b>Figure S10</b> .....	S18
<b>Figure S11</b> .....	S19
<b>Figure S12</b> .....	S20

<b>Figure S13</b> .....	S21
<b>Figure S14</b> .....	S22
<b>Figure S15</b> .....	S23
<b>Figure S16</b> .....	S24
<b>Figure S17</b> .....	S25
<b>Figure S18</b> .....	S26
<b>Figure S19</b> .....	S27
<b>Figure S20</b> .....	S28
<b>Figure S21</b> .....	S29
<b>Figure S22</b> .....	S30
<b>Table S1</b> .....	S31
<b>Table S2</b> .....	S32
<b>Table S3</b> .....	S33
<b>Table S4</b> .....	S34

## **Experiments**

### **Materials**

Niobium pentachloride ( $\text{NbCl}_5$ ) and 2-Methylimidazole (2-MeIM, 99%) were purchased from Aladdin. Melamine, methanol ( $\text{CH}_3\text{OH}$ ), ethanol ( $\text{CH}_3\text{CH}_2\text{OH}$ ), acetylene black, polytetrafluoroethylene (PTFE) and activated carbon (AC) were purchased from Sinopharm Chemical Reagent Co. Ltd. in China. All the chemicals were used without further purification.

### **Structural characterization**

X-ray diffraction (XRD) were tested with a Rigaku D/MAX-RB X-ray diffractometer ( $\text{Cu K}\alpha$ , 40 kV, 20 mA). Raman spectra were conducted on a spectrometer (JY H800UV). Nitrogen adsorption/desorption isotherms were tested with an ASAP 2020 (Micromeritics) at 77 K. The specific surface areas were recorded by Brunauer–Emmett–Teller (BET) method and the pore size distributions were obtained from the desorption branches of the isotherms by the Barrett–Joyner–Halenda (BJH) model. X-ray photoelectron spectroscopy (XPS) spectra were measured on a Perkin-Elmer PHI 5000C ESCA system accompanied with a twin anode  $\text{Mg K}\alpha$  (1253.6 eV) X-ray radiation. The Zeta potential of GO/g- $\text{C}_3\text{N}_4$  complex (10 mg dispersed in 50 ml deionized water) was tested by STABINO PMX 400. The morphology of products was viewed by scanning electron microscope (SEM, JEOL JEM-700F), transmission electron microscope (TEM, JEOL JEM-200CX), and high-resolution transmission electron

microscopy (HRTEM, JEOL JEM-2010F). The hydrophilicity of the electrode surface was analyzed the dynamic contact angle (Kruss DSA100).

### **Electrochemical characterization**

Cyclic voltammetry (CV), electrochemical impedance spectroscopy (EIS), and galvanostatic charge-discharge (GCD) were tested in a 0.5 M NaCl solution by electrochemical workstations of CHI 760D (Shanghai Chen Hua, China). The working electrode was with a size of 2 cm × 2 cm × 0.01 cm and the mass was about 5 mg. Besides, the counter electrode was a graphite sheet, and the reference electrode was the saturated calomel electrode. The frequency of EIS was from 100000 to 0.01 HZ. CV curves were tested from 1, 5, 10, 20, 50 to 100 mV s<sup>-1</sup> at the voltage window from -0.5 to 0.5 V. The current density of GCD was accepted at 0.2, 0.4, 0.6, 0.8, 1.0, and 1.2 A g<sup>-1</sup>. The specific capacitance (C<sub>m</sub>: F g<sup>-1</sup>) was calculated by the following equation

$$C_m = \left( \int IdV \right) / 2v\Delta Vm \quad (S1)$$

where I is the current density, ΔV is the voltage change, v is the scan rate, and m is the weight of the working electrode.

The contributions of the capacitive charge and the diffusion-controlled charge were obtained by the following equation

$$i(v) = k_1v + k_2v^{0.5} \quad (S2)$$

where i is the current, v is the scanning rate, k<sub>1</sub> and k<sub>2</sub> are the constant values at a fixed potential, k<sub>1</sub>v corresponds to the capacitive current, and k<sub>2</sub>v is related to the diffusion-controlled charge.

The diffusion coefficient ( $D_{\text{Na}^+}$ :  $\text{cm}^2 \text{s}^{-1}$ ) was calculated by the following equation

$$D_{\text{Na}^+} = \frac{R^2 T^2}{2n^4 c^2 F^4 A^2 \sigma^2} \quad (\text{S3})$$

$$Z_{re} = \sigma \omega^{-1/2} \quad (\text{S4})$$

where R is the gas constant, T is the absolute temperature, n is the electrons per molecule in intercalation process, c is the concentration of  $\text{Na}^+$  in the material, F is the Faraday constant, A is the surface area of the electrode,  $\sigma$  is the Warburg factor, and  $Z_{re}$  is the real part impedance.

### CDI test

The CDI electrodes were obtained by combining active materials with acetylene black and PTFE with the weight ratio of 8 : 1 : 1 and then casting into a graphite sheet with a size of 5 cm  $\times$  5 cm  $\times$  0.01 cm. After that, the electrode was dried at 80 °C overnight. The weight of active materials was about 0.072 g. The counter electrode was obtained by the same procedure with activated carbon (AC). Finally, the electrodes ( $\text{Nb}_2\text{O}_5@N\text{-C-1//AC}$ ) were assembled into a home-made desalination device to test ion adsorption performance. The two CDI electrodes were separated by a spacer. A 50 mL NaCl solution was driven cyclically through the electrodes via a peristaltic pump. A conductivity meter (SevenMulti, METTLER TOLEDO, America) was used to monitor the conductivity of the NaCl solution instantly. The applied voltage was from 0.8, 1.0 to 1.2 V and the initial concentration of NaCl solution was from 100, 300 to 500 mg  $\text{L}^{-1}$ . The flow rate was kept at 40 mL  $\text{min}^{-1}$ . The testing temperature in the capacitive

deionization experiment was maintained at 25 °C. The ion adsorption capacity (IAC) of electrodes was calculated by the following equation

$$IAC = (C_0 - C_t)V/m \quad (S5)$$

where  $C_0$  is the initial concentration,  $C_t$  is the final concentration,  $V$  is the volume of NaCl solution, and  $m$  is the total weight of active materials.

The ion adsorption rate (IAR) was calculated as:

$$IAR = IAC / t \quad (S6)$$

where  $t$  is the desalination time.

The average ion adsorption rate (AIAR) was calculated by averaging the whole IAR among the capacitive deionization time.

The concentration reduction (CR) could be calculated as:

$$CR = \frac{C_0 - C_t}{M} \quad (S7)$$

where  $M$  is the mole weight of NaCl.

The deionization rate (DR%) was calculated as:

$$DR\% = (C_0 - C_t)/C_0 \times 100\% \quad (S8)$$

The charge efficiency ( $\Lambda$ , %) was calculated by the following equation

$$\Lambda = \frac{\Gamma \times F}{\Sigma} \quad (S9)$$

where  $\Gamma$  is the removal capacity,  $F$  is the Faraday constant, and  $\Sigma$  is obtained by integrating current curves.

The specific energy consumption (SEC<sup>-1</sup>) in the constant-voltage CDI system could be calculated by the following equation

$$SEC^{-1} = \frac{(C_0 - C_t)V}{V_d \int_0^t I dt} \quad (S10)$$

where  $V_d$  is the applied voltage, and  $I$  is the time-dependent current.

The water recovery (WR) could be calculated by the following equation

$$WR = \frac{V_1 t_1}{V_1 t_1 + V_2 t_2} \quad (S11)$$

where  $V_1$  is the volume of initial NaCl solution,  $t_1$  is the desalination time in one cycle,  $V_2$  is the volume of NaCl solution recover to the initial level,  $t_2$  is the recovery time in one cycle. In the system, the ions removal/regeneration was kept in a constant volume,  $V_1=V_2$ .

The energy consumption (EC) could be calculated as:

$$EC = \frac{V_d \int_0^t I dt}{m} \quad (S12)$$

The deionized product water-specific Gibbs free energy ( $\square g$ ) was given by the following equation

$$\square g = vRT \left\{ \frac{C_0}{WR} \ln \left[ \frac{C_0 - C_t WR}{C_0(1 - WR)} \right] - C_t \ln \left[ \frac{C_0 - C_t WR}{C_t(1 - WR)} \right] \right\} \quad (S13)$$

where  $v$  is a van't Hoff factor,  $R$  is the ideal gas constant, and  $T$  is the absolute temperature.

The energy efficiency (EE) could be given by the following equation

$$EE = \frac{\square g}{EC} \quad (S14)$$

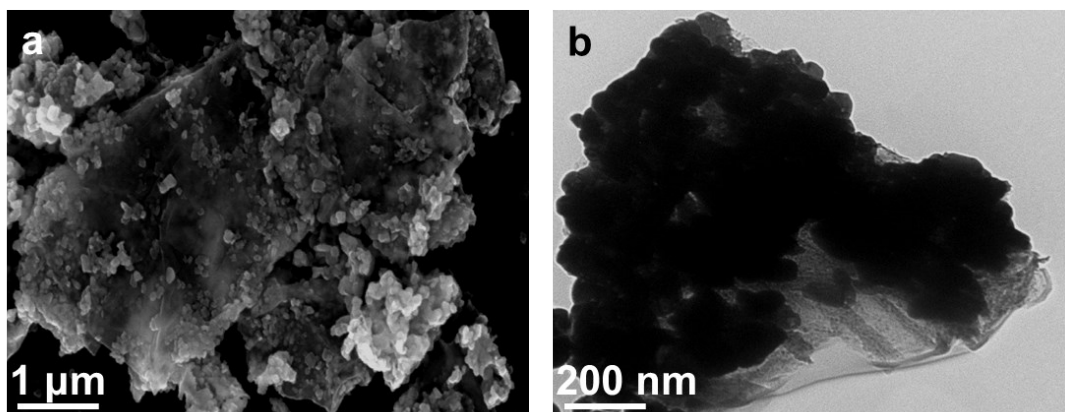


**Figure S1.** (a) SEM image and (b) TEM image of Nb/2MeIM/g-C<sub>3</sub>N<sub>4</sub>/GO precursors.

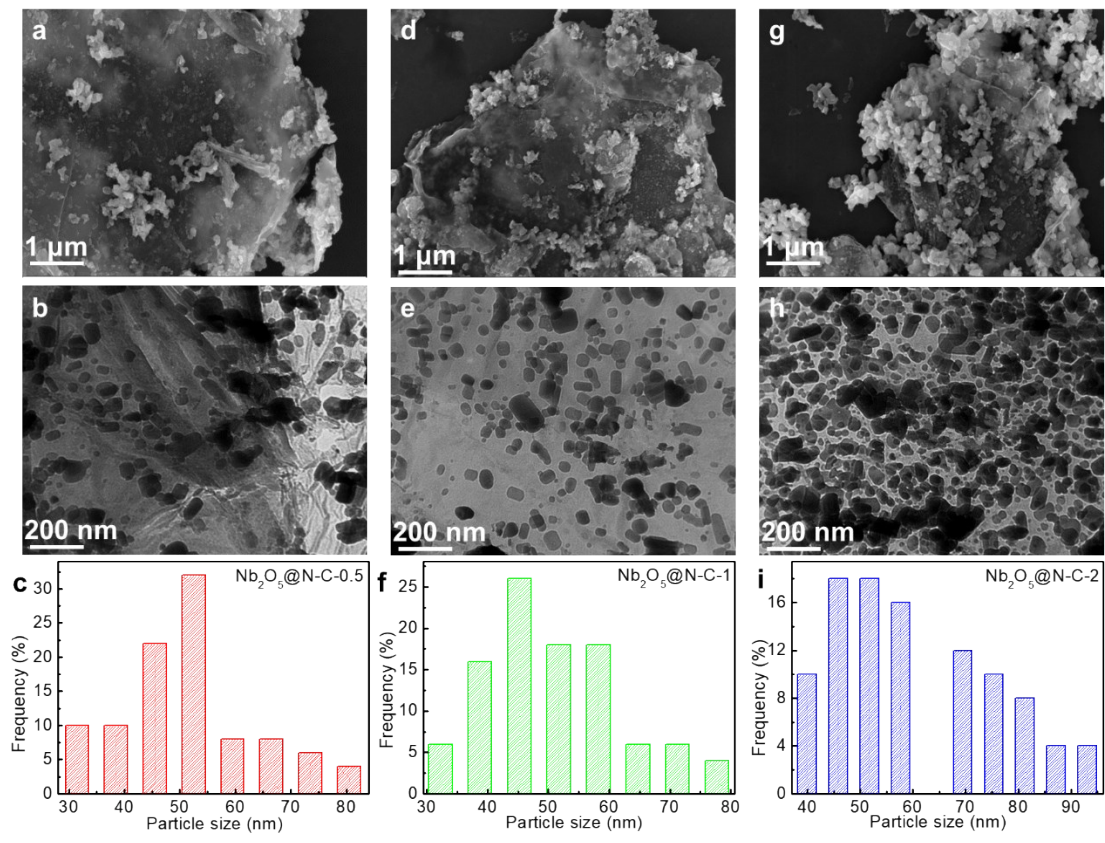


**Figure S2.** SEM image, TEM image, and particle size distribution of Nb<sub>2</sub>O<sub>5</sub>@N-C-0.5 (a, b, c), Nb<sub>2</sub>O<sub>5</sub>@N-C-1 (d, e, f) and Nb<sub>2</sub>O<sub>5</sub>@N-C-2 (g, h, i).

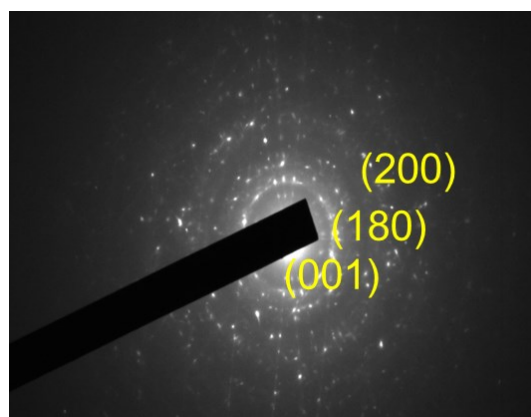


**Figure S3.** SAED pattern of Nb<sub>2</sub>O<sub>5</sub>@N-C-1.

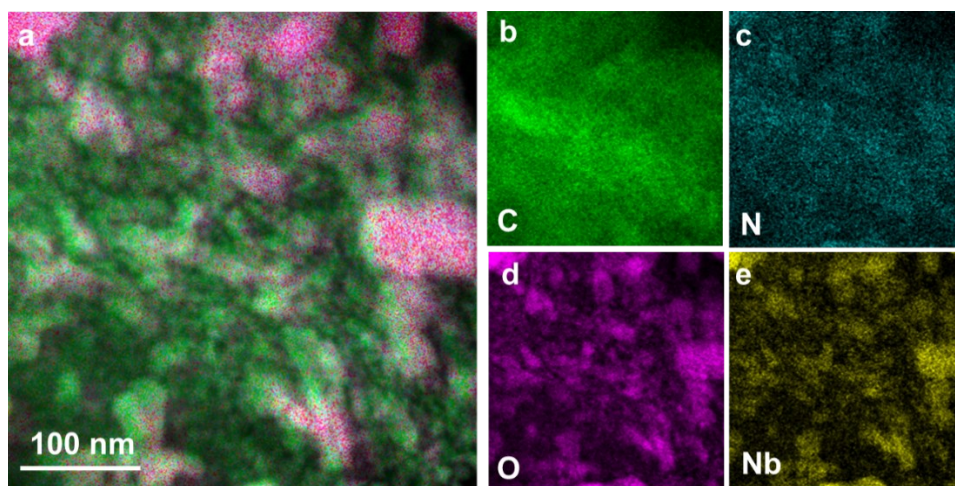


**Figure S4.** The corresponding EDS elemental mapping of C, N, O and Nb of  $\text{Nb}_2\text{O}_5@\text{N-C-1}$ .

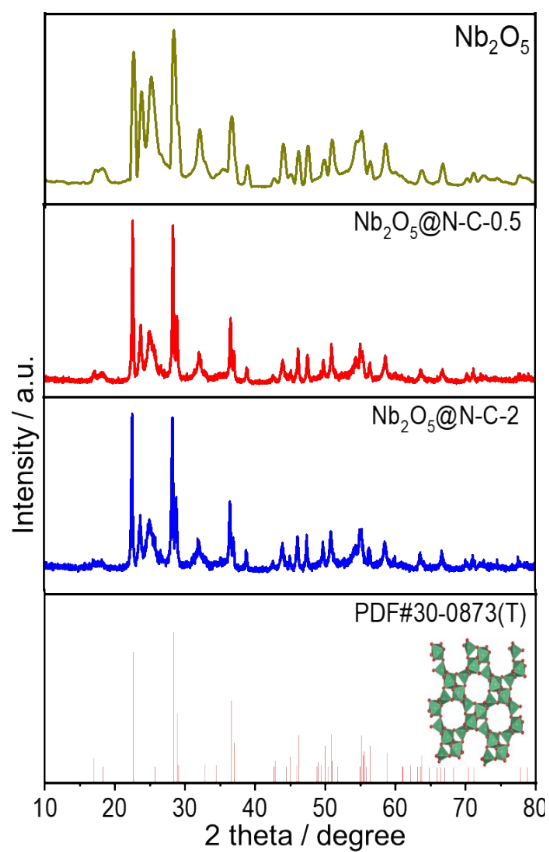


**Figure S5.** XRD patterns of bare  $\text{Nb}_2\text{O}_5$ ,  $\text{Nb}_2\text{O}_5@N-C-0.5$  and  $\text{Nb}_2\text{O}_5@N-C-2$ .

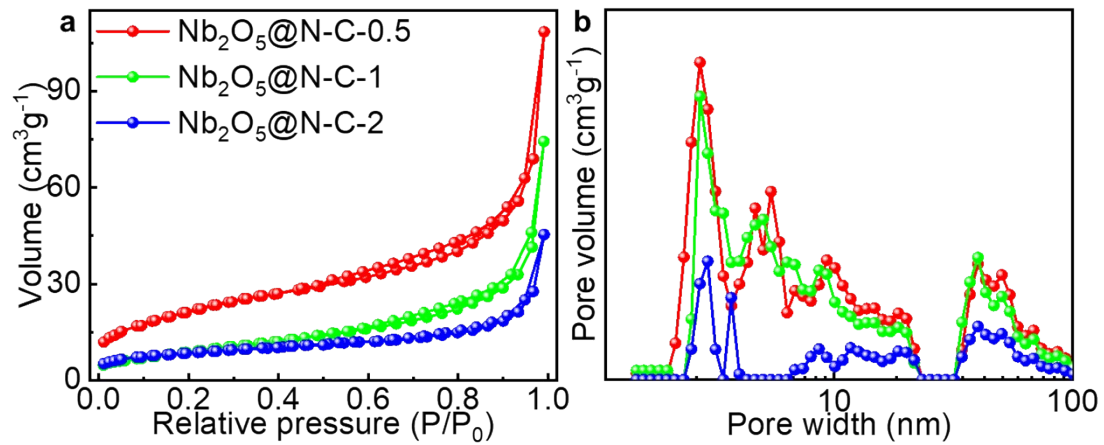


**Figure S6.** (a) N<sub>2</sub> adsorption-desorption isotherms and (b) BJH pore size distribution plots of Nb<sub>2</sub>O<sub>5</sub>@N-C-0.5, Nb<sub>2</sub>O<sub>5</sub>@N-C-1, and Nb<sub>2</sub>O<sub>5</sub>@N-C-2.

Obviously, these obtained materials demonstrated hysteresis loops in the P/P<sub>0</sub> range of 0.4-1.0, which proved the mesoporous properties.

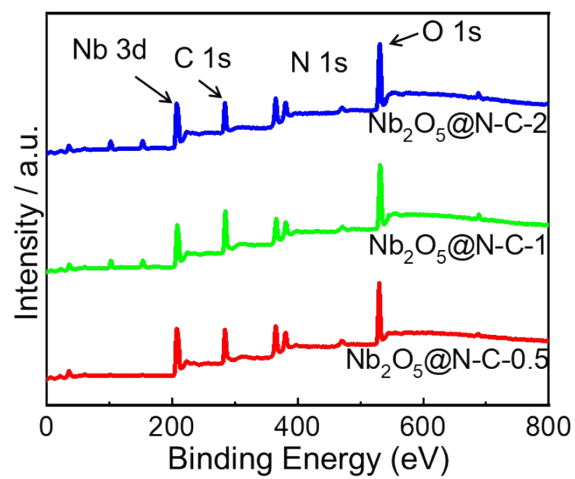


**Figure S7.** XPS survey spectra of Nb<sub>2</sub>O<sub>5</sub>@N-C-0.5, Nb<sub>2</sub>O<sub>5</sub>@N-C-1 and Nb<sub>2</sub>O<sub>5</sub>@N-C-2.

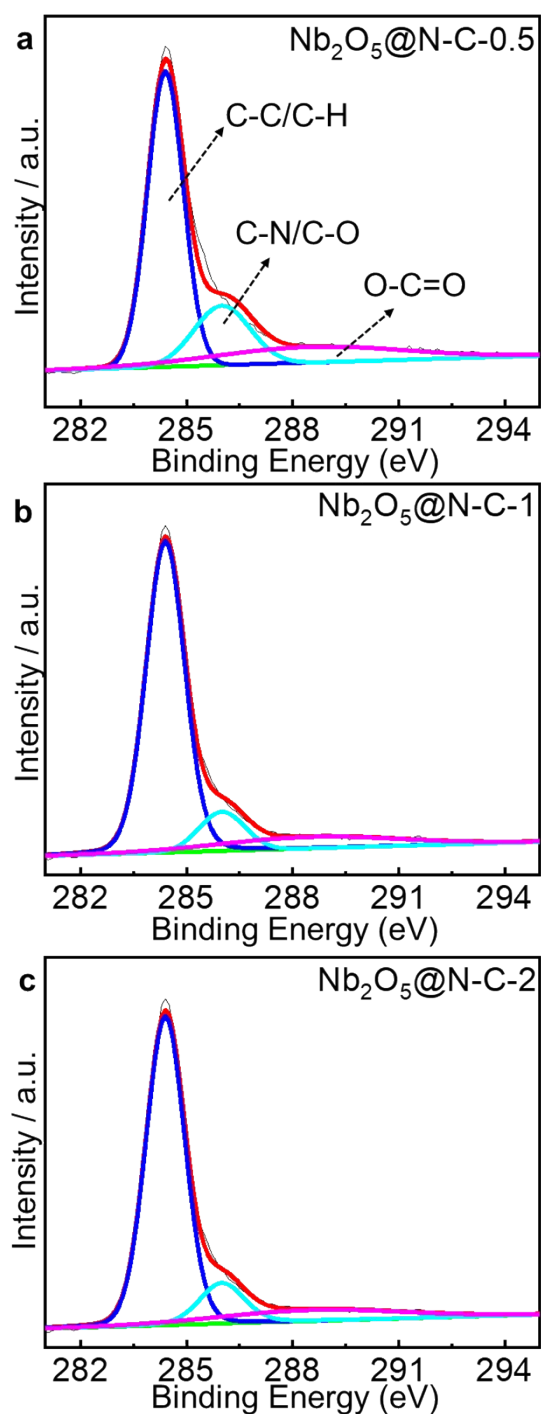


**Figure S8.** XPS spectra for C 1s of (a)  $\text{Nb}_2\text{O}_5@\text{N-C-0.5}$ , (b)  $\text{Nb}_2\text{O}_5@\text{N-C-1}$ , and (c)  $\text{Nb}_2\text{O}_5@\text{N-C-2}$ .

The high-resolution C 1s spectra could be divided into three peaks at around 284.4, 286.3, and 288.5 eV, corresponding to C-C/C-H, C-N/C-O, and O-C=O.

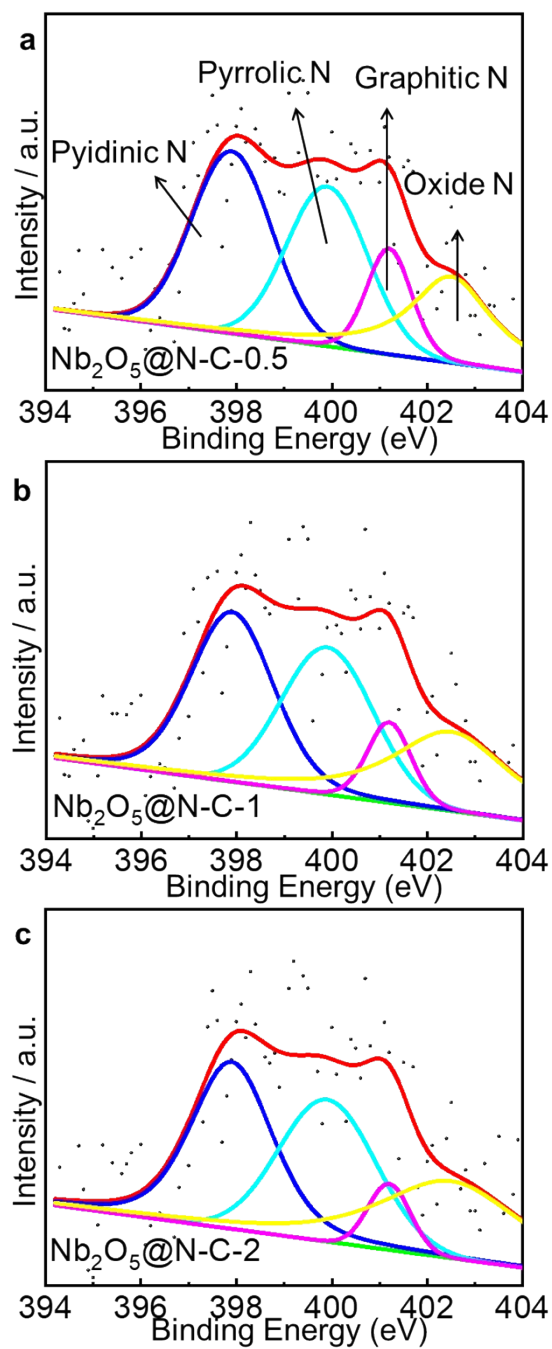


**Figure S9.** XPS spectra for N 1s of (a) Nb<sub>2</sub>O<sub>5</sub>@N-C-0.5, (b) Nb<sub>2</sub>O<sub>5</sub>@N-C-1, and (c) Nb<sub>2</sub>O<sub>5</sub>@N-C-2.

The high-resolution N 1s spectra could be deconvoluted into four peaks at around 397.9, 399.9, 401.1, and 402.8 eV, corresponding to pyridinic N, pyrrolic N, graphitic N, and oxide N.

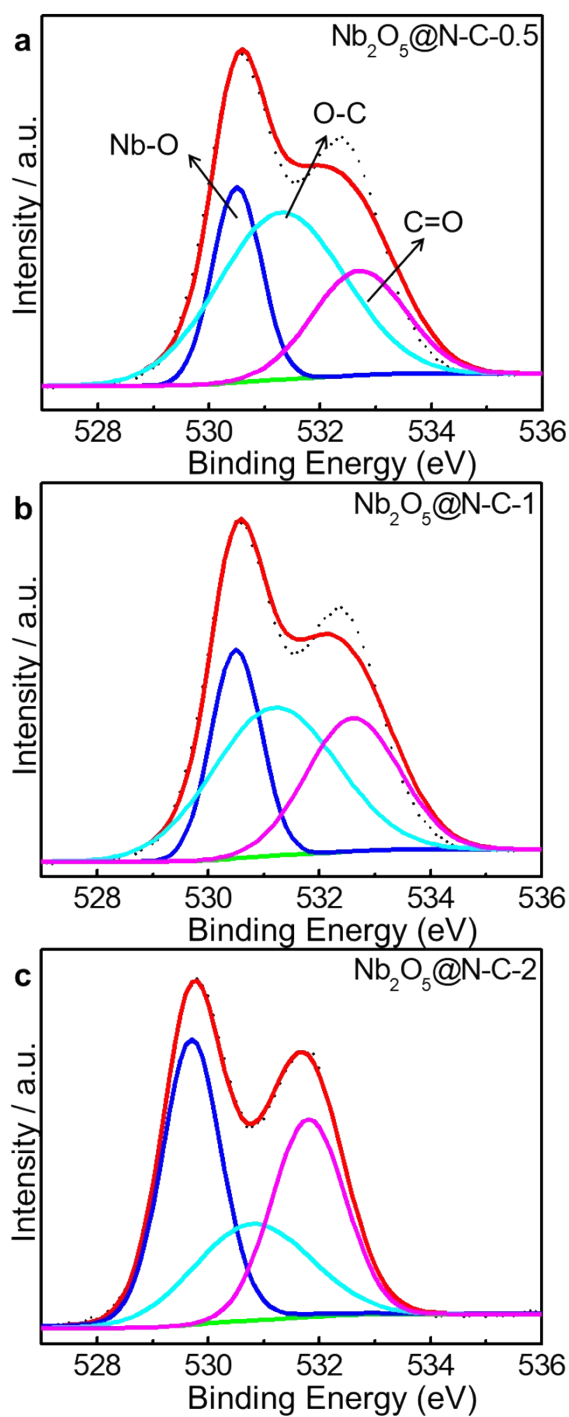


**Figure S10.** XPS spectra for O 1s of (a)  $\text{Nb}_2\text{O}_5@\text{N-C-0.5}$ , (b)  $\text{Nb}_2\text{O}_5@\text{N-C-1}$ , and (c)  $\text{Nb}_2\text{O}_5@\text{N-C-2}$ .

The high-resolution O 1s spectra could be divided into three peaks at around 530.4, 531.0, and 532.2 eV, corresponding to Nb-O, C-O and C=O. Additionally, the apparent shift to the low binding energy of  $\text{Nb}_2\text{O}_5@\text{N-C-2}$  was due to the more Nb element affecting the O binding information.

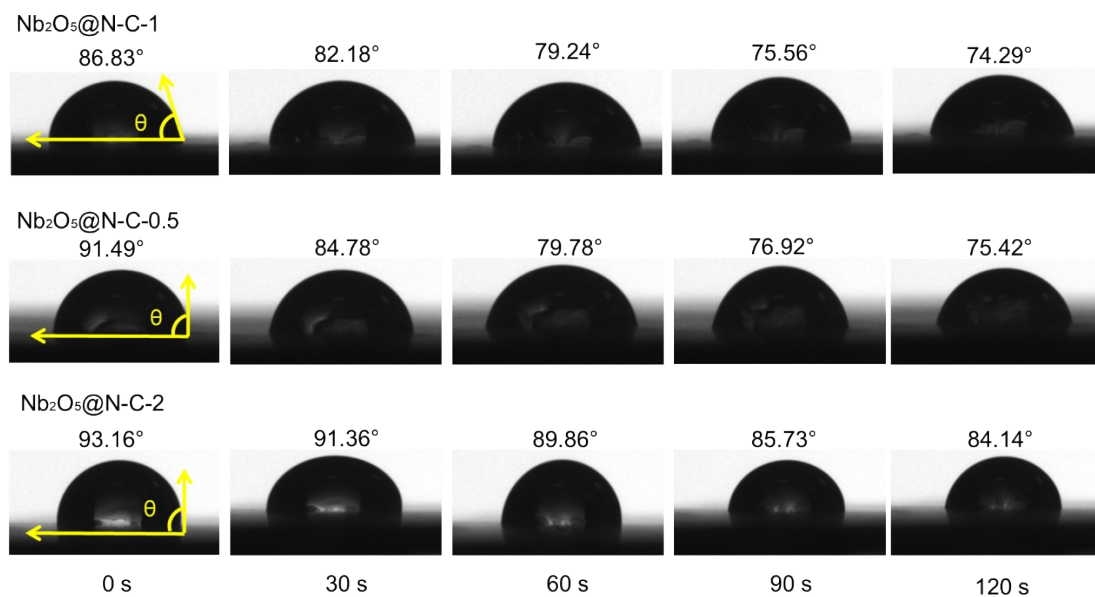


**Figure S11.** Dynamic water contact angle analysis from 0, 30, 60, 90 to 120 s of Nb<sub>2</sub>O<sub>5</sub>@N-C-0.5, Nb<sub>2</sub>O<sub>5</sub>@N-C-1, and Nb<sub>2</sub>O<sub>5</sub>@N-C-2.

When the water droplet first went close to the surface of electrodes, the contact angle of Nb<sub>2</sub>O<sub>5</sub>@N-C-1 (86.83°) was smaller than Nb<sub>2</sub>O<sub>5</sub>@N-C-0.5 (91.49°) and Nb<sub>2</sub>O<sub>5</sub>@N-C-2 (93.16°). With the test going on, the contact angle of Nb<sub>2</sub>O<sub>5</sub>@N-C-1 decreased quickly compared to Nb<sub>2</sub>O<sub>5</sub>@N-C-0.5 and Nb<sub>2</sub>O<sub>5</sub>@N-C-2. After 120 s, the Nb<sub>2</sub>O<sub>5</sub>@N-C-1 electrode reached the smallest contact angle.

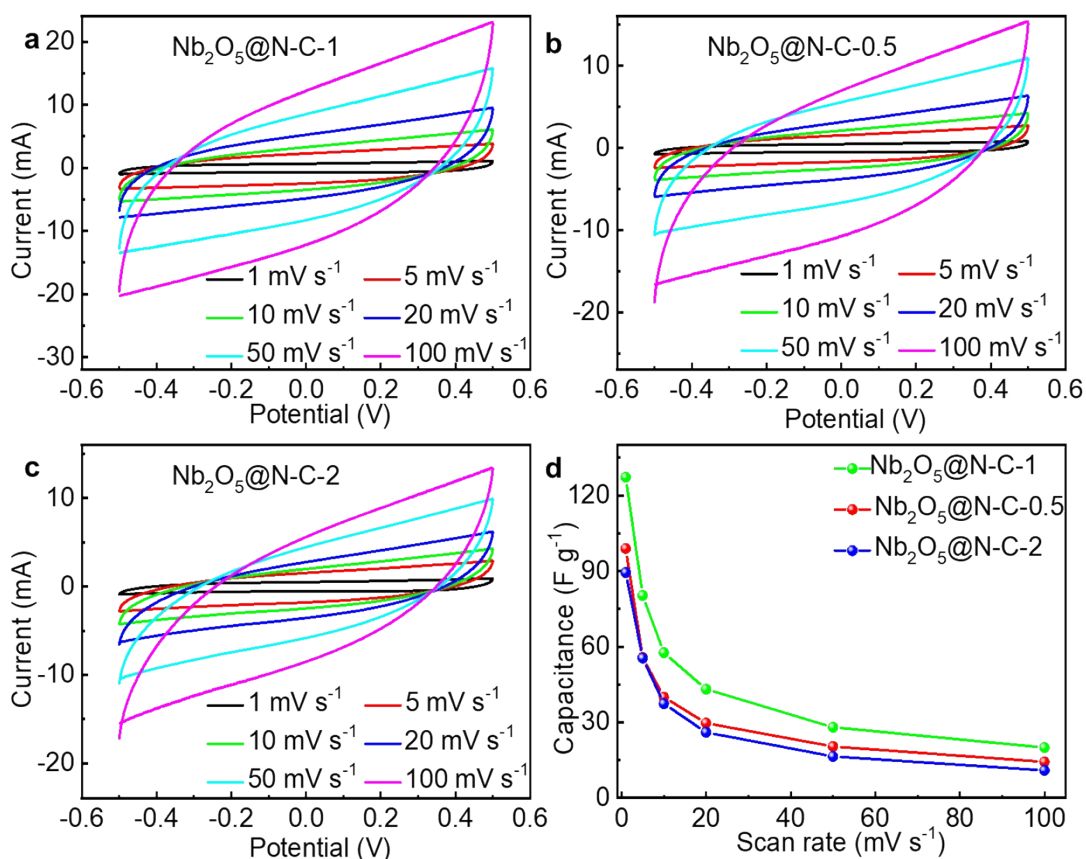


**Figure S12.** CV curves of (a) Nb<sub>2</sub>O<sub>5</sub>@N-C-1, (b) Nb<sub>2</sub>O<sub>5</sub>@N-C-0.5, and (c) Nb<sub>2</sub>O<sub>5</sub>@N-C-2 at scan rates from 1, 5, 10, 20, 50 to 100 mV s<sup>-1</sup> and (d) Specific capacitance of Nb<sub>2</sub>O<sub>5</sub>@N-C-1, Nb<sub>2</sub>O<sub>5</sub>@N-C-0.5, and Nb<sub>2</sub>O<sub>5</sub>@N-C-2 at different scan rates.

It was clear that the specific capacitance gradually decreased with scan rate increasing from 1, 5, 10, 20, 50 to 100 mV s<sup>-1</sup>. The specific capacitance of Nb<sub>2</sub>O<sub>5</sub>@N-C-1 was 127.26 (1 mV s<sup>-1</sup>), 80.32 (5 mV s<sup>-1</sup>), 57.65 (10 mV s<sup>-1</sup>), 43.13 (20 mV s<sup>-1</sup>), 28.04 (50 mV s<sup>-1</sup>), and 19.98 F g<sup>-1</sup> (100 mV s<sup>-1</sup>), higher than Nb<sub>2</sub>O<sub>5</sub>@N-C-0.5 (98.96, 55.71, 39.98, 29.7, 20.42, and 14.27 F g<sup>-1</sup>) and Nb<sub>2</sub>O<sub>5</sub>@N-C-2 (89.44, 55.47, 37.39, 26.03, 16.45, and 10.94 F g<sup>-1</sup>) at any corresponding scan rate.

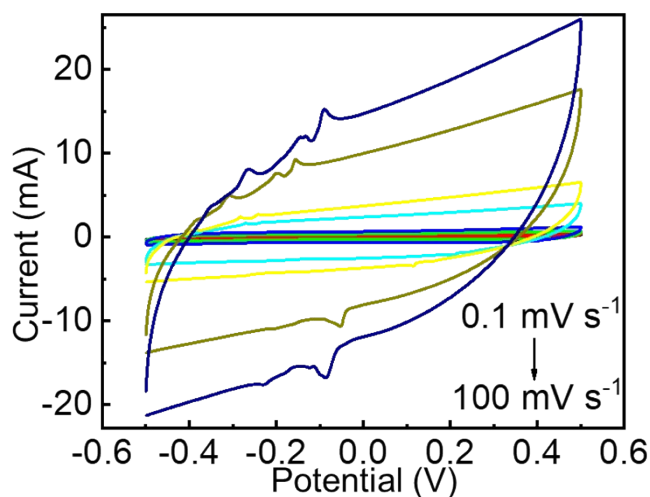


**Figure S13.** CV curves of Nb<sub>2</sub>O<sub>5</sub>@N-C-1 at scan rates from 0.1, 0.2, 0.5, 1, 5, 10, 20, 50 to 100 mV s<sup>-1</sup> (Pt foil as counter electrode).

We tested the CV measurement by a three-electrode system in a 0.5 M NaCl solution consisting of Nb<sub>2</sub>O<sub>5</sub>@N-C-1 (working electrode), Pt foil (counter electrode) and a calomel electrode (reference electrode) at scanning rates from 0.1, 0.2, 0.5, 1, 5, 10, 20, 50 to 100 mV s<sup>-1</sup>. Obviously, redox peaks were appeared at the voltage range and the peak intensity was increased with the raise of scan rates, which demonstrated a faradaic reaction of Na<sup>+</sup> ions inserting into the Nb<sub>2</sub>O<sub>5</sub>@N-C-1 electrode.

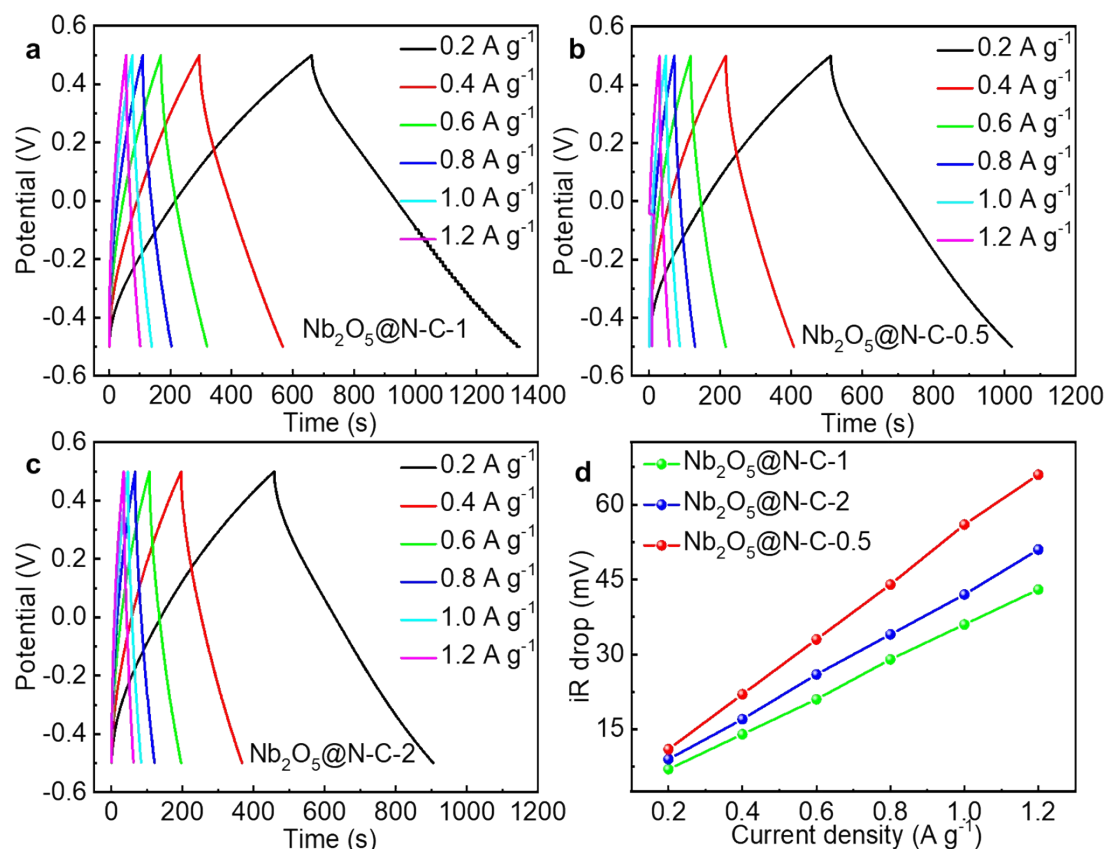


**Figure S14.** GCD curves of (a) Nb<sub>2</sub>O<sub>5</sub>@N-C-1, (b) Nb<sub>2</sub>O<sub>5</sub>@N-C-0.5, and (c) Nb<sub>2</sub>O<sub>5</sub>@N-C-2 at current densities from 0.2, 0.4, 0.6, 0.8, 1.0 to 1.2 A g<sup>-1</sup> and (d) IR drop of Nb<sub>2</sub>O<sub>5</sub>@N-C-1, Nb<sub>2</sub>O<sub>5</sub>@N-C-0.5, and Nb<sub>2</sub>O<sub>5</sub>@N-C-2 at different current density.

The iR drop increased linearly with the increase of current density from 0.2, 0.4, 0.6, 0.8, 1.0 to 1.2 A g<sup>-1</sup>. The iR drop value of Nb<sub>2</sub>O<sub>5</sub>@N-C-1 was 7 (0.2 A g<sup>-1</sup>), 14 (0.4 A g<sup>-1</sup>), 21 (0.6 A g<sup>-1</sup>), 29 (0.8 A g<sup>-1</sup>), 36 (1.0 A g<sup>-1</sup>), and 43 mV (1.2 A g<sup>-1</sup>), much smaller than Nb<sub>2</sub>O<sub>5</sub>@N-C-0.5 (9, 17, 26, 34, 42, and 51 mV) and Nb<sub>2</sub>O<sub>5</sub>@N-C-2 (11, 22, 33, 44, 56, and 66 mV) at any corresponding current density.

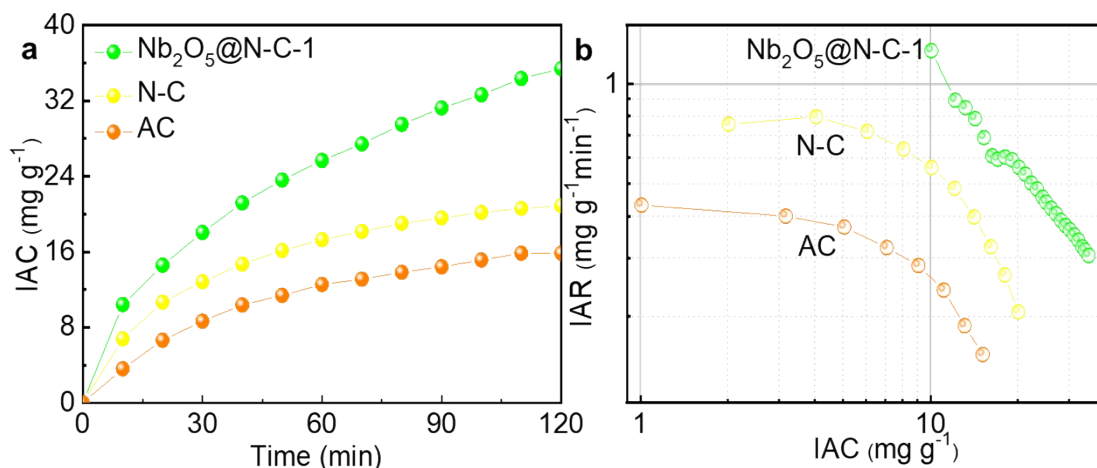


**Figure S15.** (a) Plots of IAC vs. deionization time of  $\text{Nb}_2\text{O}_5@\text{N-C-1}$ , N-C and AC electrodes in a  $500 \text{ mg L}^{-1}$  NaCl solution with a working voltage of 1.2 V and flow rate of  $40 \text{ mL min}^{-1}$ , (b) Ragone plots of IAR vs. IAC of  $\text{Nb}_2\text{O}_5@\text{N-C-1}$ , N-C and AC electrodes in a  $500 \text{ mg L}^{-1}$  NaCl solution with a working voltage of 1.2 V and flow rate of  $40 \text{ mL min}^{-1}$ .

We compared  $\text{Nb}_2\text{O}_5@\text{N-C-1}//\text{AC}$  electrodes with N-C//AC and AC//AC to prove the outstanding composite to combine  $\text{Nb}_2\text{O}_5$  with a nitrogen-doped carbon matrix. The  $\text{Nb}_2\text{O}_5@\text{N-C-1}//\text{AC}$  composites demonstrated the best removal performance of  $35.4 \text{ mg g}^{-1}$  in 120 min measurement. Nevertheless, the IAC of N-C//AC and AC//AC was merely 20.9 and  $15.8 \text{ mg g}^{-1}$ , respectively. Moreover, the Ragone plots of  $\text{Nb}_2\text{O}_5@\text{N-C-1}//\text{AC}$  also located the most upper and right region compared to other samples, indicating the fastest IAR and the largest IAC.

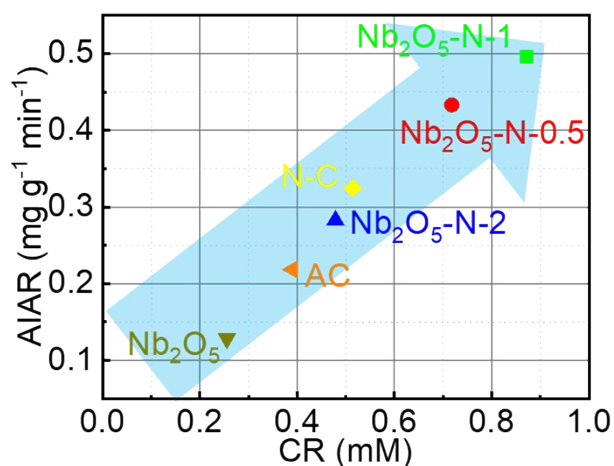


**Figure S16.** Comparison of AIAR and CR of different electrode materials in a 500 mg L<sup>-1</sup> NaCl solution with working voltage of 1.2 V and flow rate of 40 mL min<sup>-1</sup>.

The Nb<sub>2</sub>O<sub>5</sub>@N-C-1//AC indicated the biggest concentration reduction (0.88 mM) and average ion adsorption rate (0.50 mg g<sup>-1</sup> min<sup>-1</sup>) in the comparison of Nb<sub>2</sub>O<sub>5</sub>@N-C-0.5//AC (0.72 mM, 0.44 mg g<sup>-1</sup> min<sup>-1</sup>), Nb<sub>2</sub>O<sub>5</sub>@N-C-2//AC (0.48 mM, 0.29 mg g<sup>-1</sup> min<sup>-1</sup>), Nb<sub>2</sub>O<sub>5</sub>//AC (0.26 mM, 0.12 mg g<sup>-1</sup> min<sup>-1</sup>), N-C//AC (0.52 mM, 0.33 mg g<sup>-1</sup> min<sup>-1</sup>) and AC//AC (0.40 mM, 0.22 mg g<sup>-1</sup> min<sup>-1</sup>).

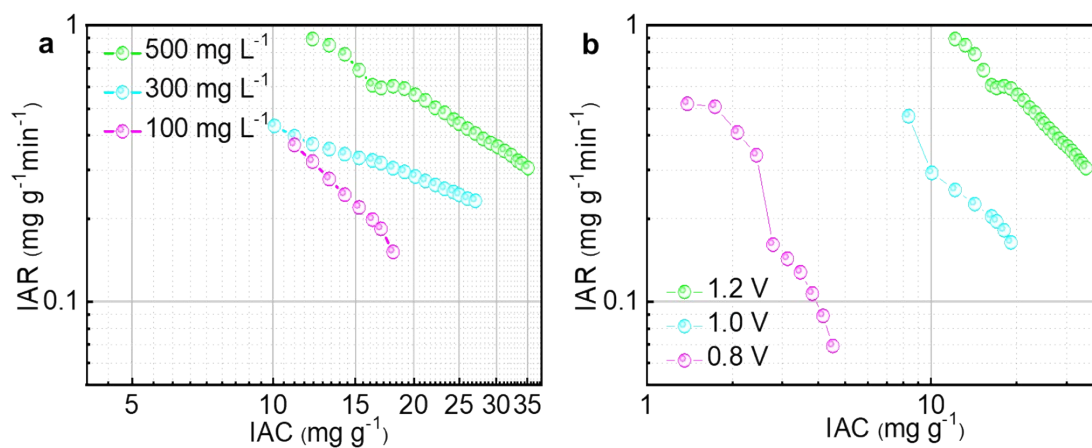


**Figure S17.** (a) Ragone plots of IAR vs. IAC of Nb<sub>2</sub>O<sub>5</sub>@N-C-1 in different initial concentrations of NaCl solution, (b) Ragone plots of IAR vs. IAC of Nb<sub>2</sub>O<sub>5</sub>@N-C-1 with different working voltages.

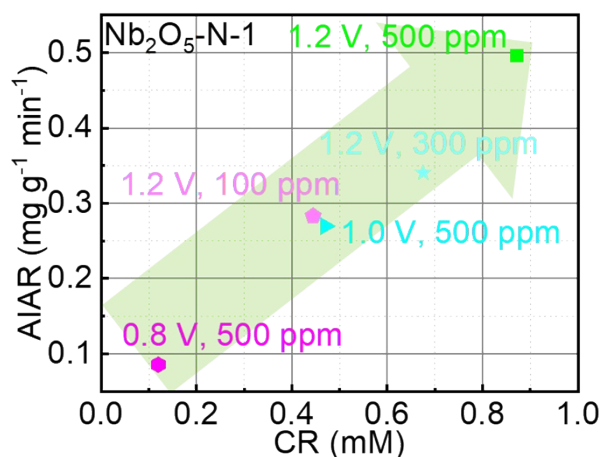


**Figure S18.** Comparison of AIAR and CR of  $\text{Nb}_2\text{O}_5@\text{N-C-1}$  in different applied voltage and initial concentration.

Different measuring parameters led to different desalination results. The  $\text{Nb}_2\text{O}_5@\text{N-C-1}/\text{AC}$  was tested in a  $500 \text{ mg L}^{-1}$  NaCl solution at 1.2 V (1.2 V, 500 ppm) indicated the biggest concentration reduction (0.88 mM) and average ion adsorption rate ( $0.50 \text{ mg g}^{-1} \text{ min}^{-1}$ ) in the comparison of 1.2 V, 300 ppm (0.68 mM,  $0.35 \text{ mg g}^{-1} \text{ min}^{-1}$ ), 1.2 V, 100 ppm (0.45 mM,  $0.29 \text{ mg g}^{-1} \text{ min}^{-1}$ ), 1.0 V, 500 ppm (0.48 mM,  $0.27 \text{ mg g}^{-1} \text{ min}^{-1}$ ), and 0.8 V, 500 ppm (0.12 mM,  $0.09 \text{ mg g}^{-1} \text{ min}^{-1}$ ).

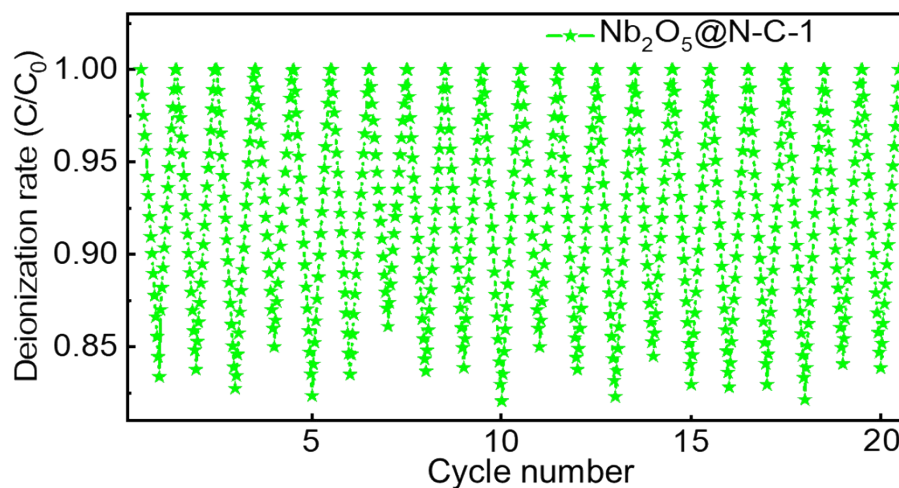


**Figure S19.** Deionization stability of Fe-N-C electrode of 20 adsorption-desorption cycles in a 100 mg L<sup>-1</sup> NaCl solution at charge/discharge voltage of 1.2-0 V and flow rate of 40 mL min<sup>-1</sup>.

From the results of desalination tests in Figure 4, we could get the conclusion that the ion adsorption occurred quickly in the first 10 min. After that, it became slowly and mildly increasing. Based on that, we accepted the ion adsorption time of 10 min and ion desorption time of 20 min.

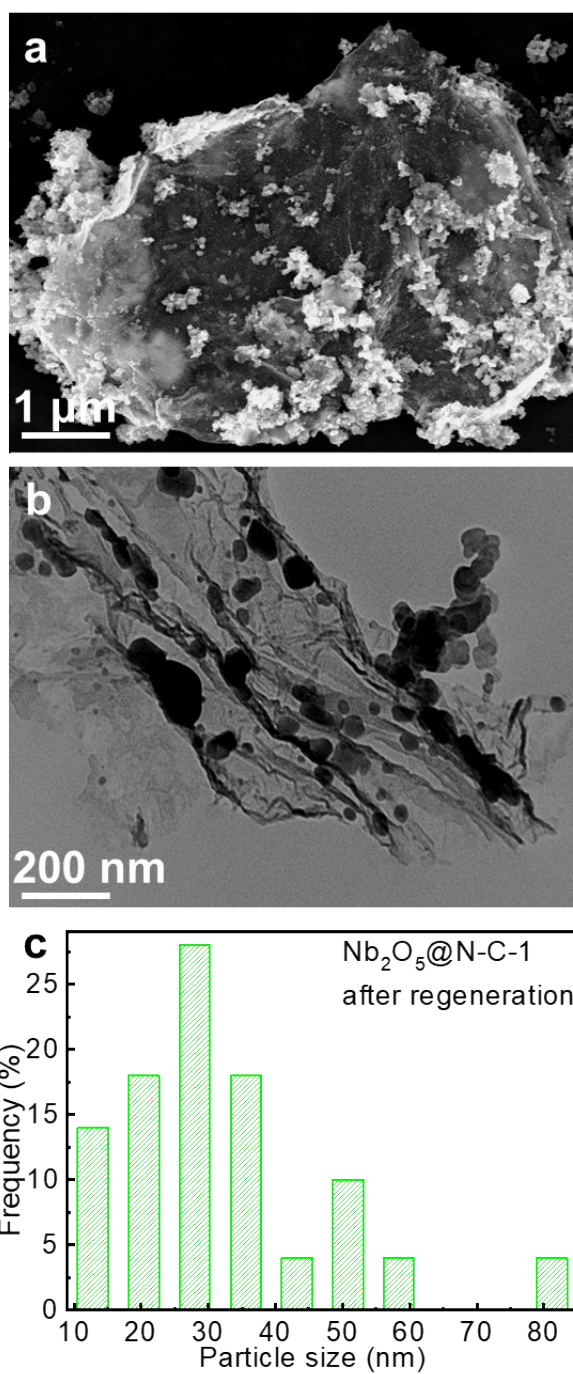


**Figure S20.** (a) SEM image, (b) TEM image, and (c) particle size distribution of  $\text{Nb}_2\text{O}_5@\text{N-C-1}$  after regeneration test.

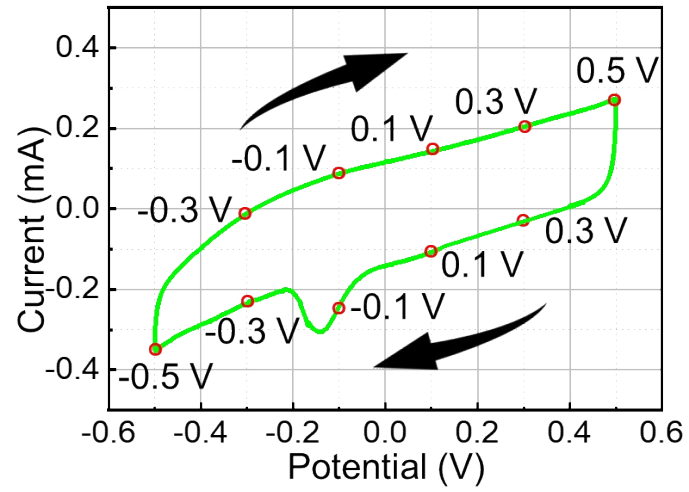


**Figure S21.** CV curves of Nb<sub>2</sub>O<sub>5</sub>@N-C-1 at 0.1 mV s<sup>-1</sup> in different stages of discharge/charge for in-situ Raman tests.

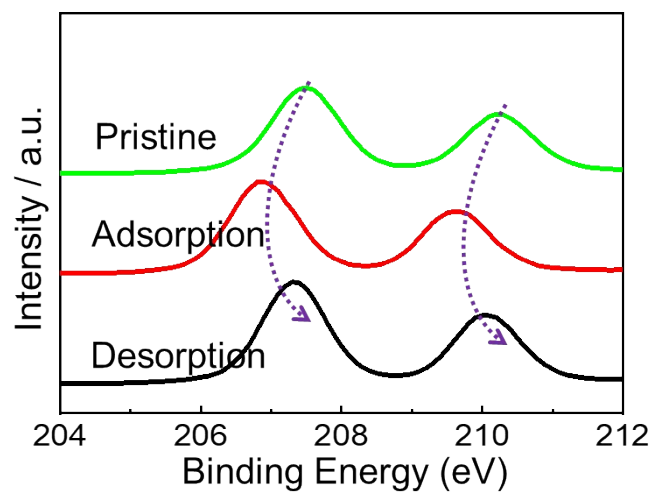


**Figure S22.** Ex-situ XPS measurements of Nb 3d peaks in different stages of pristine, adsorption, and desorption process.

**Table S1.** Specific surface area and pore volume of Nb<sub>2</sub>O<sub>5</sub>@N-C-0.5, Nb<sub>2</sub>O<sub>5</sub>@N-C-1, and Nb<sub>2</sub>O<sub>5</sub>@N-C-2.

<b>Samples</b>	<b>Nb<sub>2</sub>O<sub>5</sub>@N-C-1</b>	<b>Nb<sub>2</sub>O<sub>5</sub>@N-C-0.5</b>	<b>Nb<sub>2</sub>O<sub>5</sub>@N-C-2</b>
S <sub>BET</sub> (m <sup>2</sup> g <sup>-1</sup> )	34.1	78.6	29.5
V <sub>pore</sub> (cm <sup>3</sup> g <sup>-1</sup> )	0.13	0.17	0.07

**Table S2.** Elemental quantification analyzed by XPS of Nb<sub>2</sub>O<sub>5</sub>@N-C-0.5, Nb<sub>2</sub>O<sub>5</sub>@N-C-1, and Nb<sub>2</sub>O<sub>5</sub>@N-C-2.

<b>Samples</b>	<b>C</b>	<b>N</b>	<b>O</b>	<b>Nb</b>
Nb <sub>2</sub> O <sub>5</sub> @N-C-0.5	55.37	2.63	36.87	5.13
Nb <sub>2</sub> O <sub>5</sub> @N-C-1	52.07	4.71	35.21	8.01
Nb <sub>2</sub> O <sub>5</sub> @N-C-2	43.22	4.05	42.79	9.95

**Table S3.** The typical fitted parameters in the electrochemical impedance spectroscopy of Nb<sub>2</sub>O<sub>5</sub>@N-C-0.5, Nb<sub>2</sub>O<sub>5</sub>@N-C-1, and Nb<sub>2</sub>O<sub>5</sub>@N-C-2.

Samples	Nb <sub>2</sub> O <sub>5</sub> @N-C-1	Nb <sub>2</sub> O <sub>5</sub> @N-C-0.5	Nb <sub>2</sub> O <sub>5</sub> @N-C-2
R <sub>s</sub>	0.76	0.68	0.87
R <sub>ct</sub>	14.66	18.52	23.94

**Table S4.** Comparison of IAC of Nb<sub>2</sub>O<sub>5</sub>@N-C-1 with another metal-based electrode materials from the literature.

Electrode materials	Voltage (V)	Initial NaCl		Reference
		concentration (mg/L)	IAC (mg/g)	
Na <sub>4</sub> Mn <sub>9</sub> O <sub>18</sub>	1.2	580	31.2	S1
Na <sub>2</sub> FeP <sub>2</sub> O <sub>7</sub>	1.2	580	30.2	S2
MnO <sub>2</sub>	1.4	500	14.9	S3
AC-Ti-S	1.2	500	10	S4
Hybrid-MnO <sub>2</sub>	1.2	870	27.3	S5
Ag coated carbon	1.2	585	15.6	S6
MoS <sub>2</sub> /g-C <sub>3</sub> N <sub>4</sub>	1.6	250	24.2	S7
Ti <sub>3</sub> C <sub>2</sub> -MXene	1.2	300	15.0	S8
5 wt% CeO <sub>2</sub> @GNFs	1.4	50	7.2	S9
rGO/Co <sub>3</sub> O <sub>4</sub>	1.6	500	20.2	S10
2D MXeneTi <sub>3</sub> C <sub>2</sub> T <sub>x</sub> nanosheets	1.4	500	26.8	S11
ACP/TiO <sub>2</sub> /SO <sub>3</sub> <sup>-</sup>	1.0	500	22	S12
<b>Nb<sub>2</sub>O<sub>5</sub>@N-C-1</b>	<b>1.2</b>	<b>100</b>	<b>18.1</b>	<b>This work</b>
<b>Nb<sub>2</sub>O<sub>5</sub>@N-C-1</b>	<b>1.2</b>	<b>300</b>	<b>27.4</b>	<b>This work</b>
<b>Nb<sub>2</sub>O<sub>5</sub>@N-C-1</b>	<b>1.2</b>	<b>500</b>	<b>35.4</b>	<b>This work</b>

## References:

- S1. J. Lee, S. Kim, C. Kim and J. Yoon, Hybrid capacitive deionization to enhance the desalination performance of capacitive techniques, *Energy Environ. Sci.*, 2014, **7**, 3683-3689.
- S2. S. Kim, J. Lee, C. Kim and J. Yoon,  $\text{Na}_2\text{FeP}_2\text{O}_7$  as a Novel Material for Hybrid Capacitive Deionization, *Electrochim. Acta*, 2016, **203**, 265-271.
- S3. T. Wu, G. Wang, S. Wang, F. Zhan, Y. Fu, H. Qiao and J. Qiu, Highly Stable Hybrid Capacitive Deionization with a  $\text{MnO}_2$  Anode and a Positively Charged Cathode, *Environ. Sci. Technol. Lett.*, 2018, **5**, 98-102.
- S4. B. H. Min, J.-H. Choi and K. Y. Jung, Improved capacitive deionization of sulfonated carbon/titania hybrid electrode, *Electrochim. Acta*, 2018, **270**, 543-551.
- S5. B. W. Byles, D. A. Cullen, K. L. More and E. Pomerantseva, Tunnel structured manganese oxide nanowires as redox active electrodes for hybrid capacitive deionization, *Nano Energy*, 2018, **44**, 476-488.
- S6. H. Yoon, J. Lee, S. Kim and J. Yoon, Hybrid capacitive deionization with Ag coated carbon composite electrode, *Desalination*, 2017, **422**, 42-48.
- S7. S. Tian, X. Zhang and Z. Zhang, Capacitive deionization with  $\text{MoS}_2/\text{g-C}_3\text{N}_4$  electrodes, *Desalination*, 2020, **479**, 114348.
- S8. J. Zhang, D.-W. Wang, W. Lv, S. Zhang, Q. Liang, D. Zheng, F. Kang and Q.-H. Yang, Achieving superb sodium storage performance on carbon anodes through an ether-derived solid electrolyte interphase, *Energy Environ. Sci.*, 2017, **10**, 370-376.
- S9. A. Yousef, A. M. Al-Enizi, I. M. A. Mohamed, M. M. El-Halwany, M. Ubaidullah and R. M. Brooks, Synthesis and characterization of  $\text{CeO}_2/\text{rGO}$  nanoflakes as electrode material for capacitive deionization technology, *Ceram. Int.*, 2020, DOI: <https://doi.org/10.1016/j.ceramint.2020.03.034>.
- S10. G. Divyapriya, K. K. Vijayakumar and I. Nambi, Development of a novel graphene/ $\text{Co}_3\text{O}_4$  composite for hybrid capacitive deionization system, *Desalination*, 2019, **451**, 102-110.
- S11. L. Guo, X. Wang, Z. Y. Leong, R. Mo, L. Sun and H. Y. Yang, Ar plasma modification of 2D MXene  $\text{Ti}_3\text{C}_2\text{T}_x$  nanosheets for efficient capacitive desalination, *FlatChem*, 2018, **8**, 17-24.
- S12. B. H. Min, J.-H. Choi and K. Y. Jung, Improvement of capacitive deionization performance via using a Tiron-grafted  $\text{TiO}_2$  nanoparticle layer on porous carbon electrode, *Korean J. Chem. Eng.*, 2018, **35**, 272-282.